Qualitative and Quantitative Improvement of Optical Tomographic Reconstructed Images via an Image-correcting Filter Scheme: Two-dimensional Case

Yong Xu[1,2], Harry L. Graber[1,2], Yaling Pei[2], and Randall L. Barbour[1,2]

[1]SUNY Downstate Medical Center and [2]NIRx Medical Technologies, LLC.

INTRODUCTION

Image quality is one of key factors that determines the practicality of an imaging scheme. Experience with diffuse optical tomography (DOT) research and applications has indicated that most image reconstruction algorithms yield blurred images because localized information from the object domain is mapped to more than one position in the image domain. To reduce the blurring in reconstructed images and improve image quality, as measured by parameters such as spatial resolution and quantitative accuracy of recovered optical coefficients, an image-correcting filter scheme was proposed [1]. An illustration depicting this scheme is shown in Figure 1. As shown in the figure, the function of an image-correcting filter is to reduce the mixing of information and to make the recovered image as nearly as possible a one-to-one correspondence between object and image pixels. The original idea of the image-correcting filter method is to borrow the concept of frequency encoding of spatial information from MR imaging and to use this strategy to label information that is "transferred" from the object to image space [1]. As discussed below, in practice we find that the method works best when applied in time domain directly, rather than in the frequency domain [2].

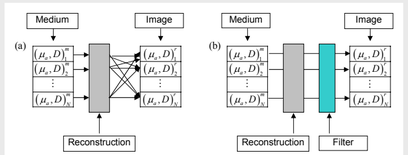

Figure 1. Panel A, schematic depicting the action of typical DOT image reconstruction algorithm, which yields blurred images because information from each object domain location is mapped to more than one position in the image domain. Panel B, the action of an ideal image-correcting filter, which is to counteract the information spreading aspect of the reconstruction algorithm's action.

An accompanying report demonstrates marked enhancement of reconstructed 3D diffuse optical tomographic images, via the image-correcting filter operation [3]. In this report, the method's performance is evaluated quantitatively; for convenience, two-dimensional test media are considered initially. The influence of several factors—geometrical disposition of sources and detectors, the fineness of the FEM mesh, the number and position of inclusions, the distance separating them, detector noise, and the optical parameter contrast between inclusion and background—have been investigated. The numerical results show that by use of the image-correcting filter scheme the quality of recovered images can be dramatically enhanced, in terms of both target geometry information such as location and size, and in the quantitative accuracy of the optical coefficients.

METHODS

The reasoning that underlay our image-correcting filter strategy, and the mathematical details of its implementation, are given in the accompanying report [3]. Here, we will briefly introduce the method in an intuitive way which is compared to the procedure of calibration of a measurement system.

We know that no measurement system is perfect. It is necessary to calibrate the system before measurement. As shown in Figure 2(a), calibration of a measurement system can be represented by the equation:

$$[S_0] = [c][S_m],$$

where $[S_0]$ and $[S_m]$ denote a series of standard signals and the corresponding measured signals, respectively, and $[c]$ are calibration coefficients. After the calibration, the measured data can be corrected by the calibration coefficients $[c]$ to acquire accurate measurements.

Similarly, for DOT imaging system, as shown in Figure 2(b), we also need to calibrate before reconstruction. Suppose the optical coefficient distribution $[\mathbf{X}_0(\mathbf{r})]$ in the spatial domain under consideration is known:

$$[\mathbf{X}_0(\mathbf{r})] = [x_{01}, x_{02}, \ldots, x_{0n}]^{\mathrm{T}},$$

where the distribution $[\mathbf{X}_0(\mathbf{r})]$ is discretized by an n-node mesh for numerical computations. Taking the known distribution as the input for the imaging system, we can obtain the reconstructed distribution

$$[\mathbf{X}_r(\mathbf{r})] = [x_{r1}, x_{r2}, \ldots, x_{rn}]^{\mathrm{T}}.$$

So calibration of the imaging system can be performed by computing $[\mathbf{X}_0(\mathbf{r})] = [F]\,[\mathbf{X}_r(\mathbf{r})]$, where the calibration coefficient $[F]$ is an $n\times n$ matrix and is called image-correcting filter. In practice, the basic steps to generate an image-correcting filter are as follows:

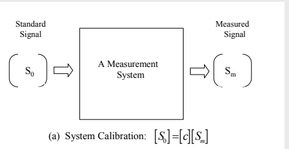

Figure 2. Analogy between the calibration of a measurement system and the image-correcting filter scheme.

(1) Generate N independently known optical coefficient distributions by computer:

$$\left[\mathbf{X}_0^{(i)}(\mathbf{r})\right] = \left[x_{01}^{(i)}, x_{02}^{(i)}, \cdots, x_{0n}^{(i)}\right]^{\mathrm{T}} \qquad i = 1,2,\cdots,N$$

where $N \geq n$;

(2) Use the forward model [4,5] to simulate the detector readings from the known distributions;

(3) Reconstruct the optical coefficient distributions from the simulated detector readings by use of the inverse model:

$$\left[\mathbf{X}_r^{(i)}(\mathbf{r})\right] = \left[x_{r1}^{(i)}, x_{r2}^{(i)}, \cdots, x_{rn}^{(i)}\right]^{\mathrm{T}} \qquad i = 1,2,\cdots,N$$

(4) Solve the matrix equation to determine the image-correcting filter:

$$\begin{bmatrix} x_{01}^{(1)} & x_{01}^{(2)} & \cdots & x_{01}^{(N)} \\ x_{02}^{(1)} & x_{02}^{(2)} & \cdots & x_{02}^{(N)} \\ \vdots & \vdots & \ddots & \vdots \\ x_{0n}^{(1)} & x_{0n}^{(2)} & \cdots & x_{0n}^{(N)} \end{bmatrix} = \begin{bmatrix} f_{11} & f_{12} & \cdots & f_{1n} \\ f_{21} & f_{22} & \cdots & f_{2n} \\ \vdots & \vdots & \ddots & \vdots \\ f_{n1} & f_{n2} & \cdots & f_{nn} \end{bmatrix} \begin{bmatrix} x_{r1}^{(1)} & x_{r1}^{(2)} & \cdots & x_{r1}^{(N)} \\ x_{r2}^{(1)} & x_{r2}^{(2)} & \cdots & x_{r2}^{(N)} \\ \vdots & \vdots & \ddots & \vdots \\ x_{rn}^{(1)} & x_{rn}^{(2)} & \cdots & x_{rn}^{(N)} \end{bmatrix}$$

Finally, any image $[\mathbf{Y}_r(\mathbf{r})]$ that is recovered using the same volume element pattern and measurement geometry as used in the generation of filter $[F]$ can be corrected by computing the matrix product $[F][\mathbf{Y}_r(\mathbf{r})]$.

The test medium geometries and source-detector configurations used for the demonstrations that are reported here are shown in Figure 3. In our FEM numerical computations, four different meshes are used for round media, which contain 717 nodes and 1368 triangular elements, 1019 nodes and 1940 triangular elements, 1610 nodes and 3090 triangular elements, and 2771 nodes and 5372 triangular elements, respectively. The first three of these meshes are used for inverse calculations and the last one for forward calculations. For rectangular media a 1025 node, 1920 triangular element mesh is used for inverse calculations, and a 3969 node, 7680 element mesh for forward calculations. All the computations in this report were conducted in a 2.4 GHz Pentium IV personal computer.

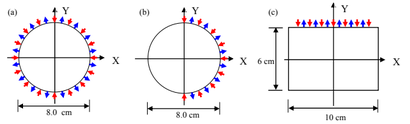

Figure 3. The test medium geometries and source-detector configurations: (a) round medium with full-tomographic measurement geometry; (b) round medium with limited view measurement geometry; (c) rectangular medium with limited view measurement geometry.

RESULTS

The qualitative and quantitative effectiveness of the image-correcting filter method are presented here by 2D simulations for both the round and the rectangular media shown in Figure 3. As the first example, the reconstructed images of one and four inclusions are shown in Figure 4, which demonstrates that the recovered image quality can be dramatically enhanced by the image-correcting filter. Then, the effects of FEM mesh fineness, inclusion/background contrast, the number of detector readings, and the positions of inclusions in the media on the reconstructed images corrected by the filters are presented in Figures 5.1-5.4, respectively. Figure 6 shows the recovered images in limited-view source-detector configurations, for both round and rectangular media. To quantitatively analyze the spatial resolution of reconstructed images under different conditions, we define the full width at half-maximum (FWHM) of the recovered image's point-spread function as the the spatial resolution of a reconstructed image as shown in Figure 7. With this definition of spatial resolution, several quantitative analyses and comparisons are given in Figures 8.1 and 8.2. The dependence of the performance of a filter on the number N of known optical coefficient distributions is investigated in Figure 9. Finally, the robustness of our image-correcting filter method is explored in Figures 10 and 11. The influence of noise on our method is shown in Figure 10. And Figure 11 examines the effect of the mismatch between the background optical properties of recovered images and the background optical properties used in filter generations on filter-corrected images.

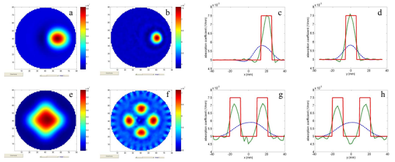

Figure 4. Reconstructed absorption images and corresponding 1D distributions: (a) one inclusion, without filter; (b) one inclusion, with filter; (c) 1D profiles of one inclusion along x=0; (d) 1D profiles of one inclusion along y=1.5; (e) four inclusions, without filter; (f) four inclusions, with filter; (g) 1D profiles of four inclusions along x=0; (h) 1D profiles of four inclusions along y=0. Here, solid (red) lines are exact distributions, dashed (green) lines are reconstructed distributions after application of filter, and dash-dot (blue) lines are reconstructed distributions before application of filter. A 32×32 full-tomographic source-detector geometry and an FEM mesh with 1019 nodes were used in these calculations.

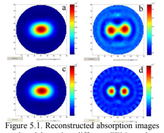

Figure 5.1. Reconstructed absorption images produced by using different FEM meshes: (a) no filter and 717-node mesh; (b) with filter and 717-node mesh; (c) no filter and 1019-node mesh; (d) with filter and 1019-node mesh.

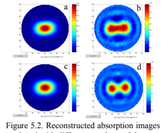

Figure 5.2. Reconstructed absorption images produced with different numbers of detector readings: (a) 16×16 readings, no filter; (b) 16×16 readings, with filter; (c) 32×32 readings, no filter; (d) 32×32 readings, with filter.

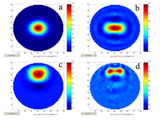

Figure 5.3. Reconstructed absorption images with different inclusion positions: (a) inclusion at y = 0, no filter; (b) inclusion at y = 0, with filter; (c) inclusion at y = 2.5, no filter; (d) inclusion at y = 2.5, with filter.

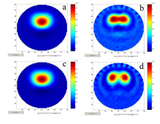

Figure 5.4. Reconstructed absorption images with different inclusion/background contrasts: (a) contrast = 1.5, no filter; (b) contrast = 1.5, with filter; (c) contrast = 3, no filter; (d) contrast = 3, with filter.

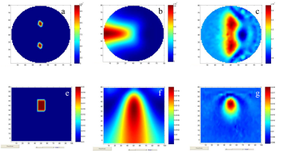

Figure 6. Reconstructed absorption images with the limited view source-detector configurations shown in Figs.3b and 3c: (a) ideal image of two inclusions in round medium; (b) recovered image of two inclusions, without filter; (c) recovered image of two inclusions, with filter; (e) ideal image of one inclusion in rectangular medium; (f) recovered image of one inclusion, without filter; (g) recovered image of one inclusion, with filter. Here, the round FEM mesh has 717 nodes and 1368 triangle elements and the rectangular mesh has 1025 nodes and 1920 triangle elements. For the round medium, 9 sources and 24 detectors are located on right semicircle as shown in Fig. 3b; for the rectangular medium, 33 sources and 33 detectors are uniformly arranged on top edge (y = 3.0), as shown in Fig. 3c.

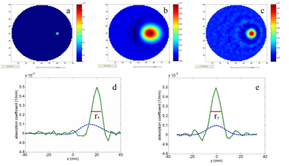

Figure 7. The definition of spatial resolution of reconstructed images: (a) ideal image of point-like inclusion at (2.0, 0); (b) recovered image of point-like inclusion without filter; (c) recovered image with filter; (d) 1D point-spread function of recovered image along x = 0; (e) 1D point-spread function of recovered image along y = 2.0. Here, the spatial resolution of reconstructed images is defined as the full width at half-maximum (FWHM) of the point-spread function, e.g., τ_x and τ_y are the resolutions of filtered image in x- and y-directions, respectively. The same mesh and source-detector geometry as those in Fig. 3 have been used in the calculations.

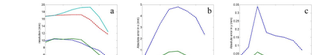

Figure 8.1. Position dependences of spatial resolution and image deviation of recovered images: (a) comparisons of resolutions of reconstructed images with and without filter, where light blue curve is the resolution without filter in the x-direction, red curve is the resolution without filter in the y-direction, green curve is the resolution with filter in the x-direction, and dark blue curve is the resolutions with filter in y-direction; (b) comparison of inclusion centroid position error with and without filter in x-direction, where blue curve is the result without filter and green curve is the results with filter; (c) comparison of inclusion centroid position error with and without filter in y-direction, where blue curve is the results without filter and green curve is the results with filter. In the calculations the same mesh and source-detector geometry as those in Fig. 3 have been used.

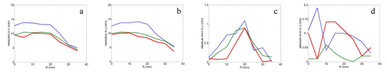

Figure 8.2. Resolution and inclusion centroid position error, as a function of the number of FEM mesh nodes: (a) resolution in x-direction for different reconstruction meshes; (b) resolution in y-direction for different reconstruction meshes; (c) centroid position error in x-direction for different reconstruction meshes; (d) centroid position error in y-direction for different reconstruction meshes. Here, all results are with image-correcting filter, and dashed (green) lines are the results for mesh with 717 nodes, dash-dot (blue) lines are the results for mesh with 1019 nodes, and solid (red) lines are the results for mesh with 1610 nodes. In the calculations, the same medium and source-detector geometry as those in Fig. 3 were used.

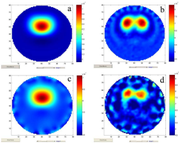

Figure 10. Effect of noise on the image-correcting filter method: (a) reconstructed image of two inclusions without noise and without filter; (b) reconstructed image of two inclusions without noise and with filter; (c) reconstructed image of two inclusions with Gaussian distributed noise (mean zero and 1% standard deviation) and without filter; (d) reconstructed image of two inclusions with Gaussian distributed noise and with filter. Here, the 32×32 full-tomographic source-detector geometry and 717-node FEM mesh have been used in the calculations. Both inclusions have inclusion/background absorption contrast of 3/1.

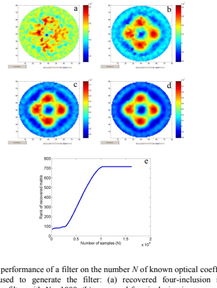

Figure 9. The performance of a filter on the number N of known optical coefficient distributions used to generate the filter: (a) recovered four-inclusion image corrected by the filter with N = 1000; (b) recovered four-inclusion image corrected by the filter with N = 5000; (c) recovered four-inclusion image corrected by the filter with N = 8000; (d) recovered four-inclusion image corrected by the filter with N = 16000; (e) the rank of recovered absorption coefficient matrix for filter generation. Here, the 16×16 full-tomographic source-detector geometry and 717-node FEM mesh have been used in calculations.

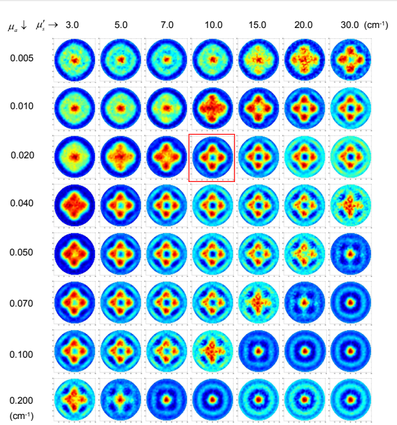

Fig. 11. Reconstructed images, produced by applying an image-correcting filter that was generated from simulations on a target medium whose properties were μ_a = 0.02 cm^{-1}, μ_s' = 10 cm^{-1}, to images reconstructed from 56 sets of detector readings obtained from test media whose background μ_a values ranged from 0.005 cm^{-1} to 0.2 cm^{-1} and whose background μ_s' values ranged from 3 cm^{-1} to 30 cm^{-1}. In each test medium μ_s' was spatially homogeneous and μ_a in the four inclusions was twice the background value.

CONCLUSIONS

In this report the image-correcting filter scheme is introduced in an intuitive way which is compared to the procedure of calibration on a measurement system [6,7]. That is, the generation of the image-correcting filter $[F]$ can be regarded as a straightforward DOT reconstruction algorithm calibration problem. The effectiveness of the method has been demonstrated by numerical simulations in 2D cases and 3D [3] cases. The qualitative and quantitative numerical results show that the image-correcting filter can significantly enhance the recovered image quality, in terms of both inclusion geometry information such as location and size, and the quantitative accuracy of the recovered optical coefficients.

REFERENCES

[1] H. L. Graber, R. L. Barbour, and Y. Pei, "Quantification and enhancement of image reconstruction accuracy by frequency encoding of spatial information," in OSA Biomedical Topical Meetings, OSA Technical Digest (Optical Society of America, Washington DC, 2002), pp. 635-637.

[2] R. L. Barbour, H. L. Graber, Y. Xu, Y. Pei, and R. Aronson, "Strategies for imaging diffusing media," *Transport Theory and Statistical Physics* (to be published).

[3] H. L. Graber, Y. Xu, Y. Pei, and R. L. Barbour, "Qualitative and quantitative improvement of optical tomographic reconstructed images via spatial deconvolution: three-dimensional case," elsewhere in this conference record.

[4] Y. Pei, Y. Pei, H. L. Graber, and R. L. Barbour, "Normalized-constraint algorithm for minimizing inter-parameter crosstalk in DC optical tomography," *Optics Express* **9**, 97–109 (2001).

[5] Y. Pei, H. L. Graber, and R. L. Barbour, "Influence of systematic errors in reference states on image quality and on stability of derived information for DC optical imaging," *Applied Optics* **40**, 5755–5769 (2001).

[6] C. L. Matson, "Deconvolution-based spatial resolution in optical diffusion tomography," *Applied Optics* **40**, 5791–5801 (2001).

[7] H. Hofer, L. Chen, Y. Yoon, B. Singer, Y. Yamauchi, and D. R. Williams, "Improvement in retinal image quality with dynamic correction of the eye's aberrations," *Optics Express* **8**, 631–643 (2001).

ACKNOWLEDGEMENT

This research was support in part by the National Institutes of Health (NIH) under Grants R21-HL67387, R21-DK63692 and R41-CA96102 and by the US Army under Grant DAMD017-03-C-0018.

I look to ***THE DIFFUSION OF LIGHT*** and education as the resource to be relied on for ameliorating the condition, promoting the virtue, and advancing the happiness of man.

— Thomas Jefferson (1822)